

The current feedback on stress modifies the Ekman buoyancy flux at fronts

Jacob O. Wengenrat

Department of Atmospheric and Oceanic Science, University of Maryland, College Park

⁴ Corresponding author: Jacob O. Wenegrat, wenegrat@umd.edu

5 ABSTRACT: Ocean surface currents introduce variations into the surface wind-stress that can
6 change the component of the stress aligned with the thermal wind shear at fronts. This modifies
7 the Ekman buoyancy flux, such that the current feedback on the stress tends to generate an
8 effective flux of buoyancy and potential vorticity to the mixed-layer. Scaling arguments and
9 idealized simulations resolving both mesoscale and submesoscale turbulence suggest that this
10 pathway for air-sea interaction can be important both locally at individual submesoscale fronts
11 with strong surface currents—where it can introduce equivalent advective heat fluxes exceeding
12 several hundred W m^{-2} —and in the spatial mean where it reduces the integrated Ekman buoyancy
13 flux by approximately 50%. The accompanying source of surface potential vorticity injection
14 suggests that at some fronts the current feedback modification of the Ekman buoyancy flux may
15 be significant in terms of both submesoscale dynamics and boundary layer energetics, with an
16 implied modification of symmetric instability growth rates and dissipation that scales similarly to
17 the energy lost through the negative wind work generated by the current feedback. This provides an
18 example of how the shift of dynamical regimes into the submesoscale may promote the importance
19 of air-sea interaction mechanisms that differ from those most active at larger scale.

20 **1. Introduction**

21 The mechanisms of air-sea interaction and coupling have been the subject of extensive study
22 at scales of 10-100 km in the ocean mesoscale. Emerging from this work is a robust picture of
23 the importance of air-sea interactions—where variability in ocean surface currents and sea-surface
24 temperature drive variability in the atmosphere which then can feedback on the ocean evolution
25 through modifications to the surface fluxes of heat and momentum (Seo et al. 2023). Interactions
26 of this type have been documented to be important across a wide-range of processes in both the
27 atmosphere and the ocean: from global climate variability such as El-Niño (Pacanowski 1987; Luo
28 et al. 2005), to basin-scale features such as the Gulf Stream path and stability (Renault et al. 2016a,
29 2019a), and down to the energetics of the ocean mesoscale eddy field which holds the majority of
30 the kinetic energy of the general circulation (Dewar and Flierl 1987; Ferrari and Wunsch 2009; Xu
31 et al. 2016; Bishop et al. 2020; Rai et al. 2021).

32 At the same time, over the last several decades it has also become evident that the surface ocean
33 is rich with variability at the submesoscale, which is best defined dynamically as flows with $O(1)$
34 Richardson and Rossby numbers (generally found at horizontal scales of 100 m to 10 km). Processes
35 at these scales are critical to both local ocean boundary layer dynamics and biogeochemistry, and
36 may play a significant role in regional, or global, integrated air-sea heat fluxes, seasonal energetics of
37 the mesoscale, and pathways between the surface and interior (Su et al. 2018; Wenegrat et al. 2018;
38 Schubert et al. 2020; Naveira Garabato et al. 2022; Taylor and Thompson 2023). Likewise many
39 features of larger-scale ocean variability, such as western boundary currents and mesoscale eddies,
40 are now recognized to have embedded sharp fronts and other features that fall in the submesoscale
41 regime (Thomas et al. 2013; Brannigan et al. 2017; Zhang and Qiu 2018). However, despite
42 the advances in understanding ocean circulation at the submesoscale, the role of submesoscale
43 variability in air-sea interaction—and whether there are significant coupled interactions at this
44 scale—remains less established.

45 Prior work using numerical modeling and observations suggest that some of the known physical
46 pathways for air-sea interaction at the ocean mesoscale are also likely active at the submesoscale.
47 This includes both thermal interactions, whereby variations in surface temperature induce changes
48 in surface winds (Wenegrat and Arthur 2018; Shao et al. 2019; Sullivan et al. 2020), and the
49 modulation of surface momentum fluxes by ocean surface currents. This last mechanism in

particular has been identified as important in ocean simulations, where inclusion of the surface current feedback on the stress (CFB) introduces anticorrelations between surface stress anomalies and surface currents that act as a damping term in the kinetic energy equation (Duhaut and Straub 2006). This ‘eddy-killing’ effect has been demonstrated to significantly modify the flux of kinetic energy between the mesoscale and submesoscale, and from the submesoscale ocean to the atmosphere (Renault et al. 2018). In this manuscript however the focus is on an alternate physical mechanism through which the CFB can also affect ocean dynamics and energetics at sharp fronts, through modifications of the cross-frontal advection of buoyancy—a key driver of submesoscale variability.

Winds blowing parallel to fronts generate a cross-front transport of buoyancy, termed the Ekman Buoyancy Flux (EBF, Thomas and Ferrari 2008). The strong buoyancy gradients at submesoscale fronts allow even moderate winds to generate extremely large magnitude EBF, with observed values exceeding the equivalent of an $O(10,000 \text{ W m}^{-2})$ surface heat flux (D’Asaro et al. 2011; Thomas et al. 2013). This advective flux overwhelms surface heat fluxes between the atmosphere and ocean, and hence is a central component of the mixed-layer buoyancy budget at fronts (Johnson et al. 2020a,b). Further, the EBF helps set the rate of the frictional surface flux of potential vorticity (PV)—a dynamical tracer—with surface PV destruction leading to submesoscale frontogenesis, the emergence of fast-growing symmetric instabilities, and the generation of extremely strong boundary layer turbulence (Thomas and Lee 2005; D’Asaro et al. 2011; Thomas et al. 2013). The purpose of this manuscript is to document how the modulation of surface momentum fluxes by ocean surface currents also introduce modulations of the EBF at submesoscale fronts, leading to an effective source of buoyancy and PV to the ocean mixed-layer which may alter the evolution of submesoscale fronts. This mechanism is likely to be significant primarily in cases of submesoscale fronts with strong surface currents, as are frequently seen within energetic larger-scale features such as western boundary currents and along the periphery of some mesoscale eddies.

The manuscript is structured as follows. In section 2 the basic theory of how the current feedback on stress modifies the surface Ekman buoyancy flux is introduced, along with scalings to determine its importance relative to the standard formulation of the EBF. In section 3 an idealized numerical model is introduced and used to validate several of the scalings and establish the quantitative effect.

79 The potential importance of this mechanism relative to other processes active at the submesoscale
80 is discussed in section 4, and results are summarized in section 5.

81 **2. Current feedback on stress and the Ekman buoyancy flux**

82 *a. Current feedback on stress*

83 The origin of the CFB is evident through a simple kinematic consideration of the surface stress,
84 which is a function of the wind-speed *relative* to the surface ocean currents. When the surface
85 current flows in the same direction as the wind, the relative wind speed (the difference in speed
86 between the atmosphere and ocean) is reduced, reducing the surface stress. In contrast, when wind
87 and currents are in opposing directions the relative wind speed is increased, and the surface stress
88 is enhanced. The bulk surface stress incorporating this effect can be written as

$$\tau = \rho_a c_d |\mathbf{U}_a - \mathbf{u}_o| (\mathbf{U}_a - \mathbf{u}_o), \quad (1)$$

89 where ρ_a is the density of air, c_d is the surface drag coefficient, \mathbf{U}_a is the surface wind vector, and
90 \mathbf{u}_o is the surface ocean current vector. From this a stress anomaly due to the CFB can be defined
91 as

$$\tau' = \tau - \underbrace{\rho_a c_d |\mathbf{U}_a| \mathbf{U}_a}_{\bar{\tau}}, \quad (2)$$

92 where $\bar{\tau}$ is the standard bulk stress defined using the earth-relative wind vector. The total wind
93 stress thus consists of a portion due solely to the winds, and an anomaly term due to the CFB.

94 It is also useful to develop approximate versions of (1) and (2) by noting that generally $|\mathbf{u}_o| \ll$
95 $|\mathbf{U}_a|$, such that terms that are quadratic in the ocean surface velocity can be neglected (Bye 1985;
96 Rooth and Xie 1992; Duhaut and Straub 2006; Renault et al. 2017)

$$\tau \approx \rho_a C_d |\mathbf{U}_a| \mathbf{U}_a - 2\rho_a c_d |\mathbf{U}_a| |\mathbf{u}_o| \mathbf{e}, \quad (3)$$

97 where $\mathbf{e} = \cos \theta \mathbf{i} + 0.5 \sin \theta \mathbf{j}$, with (\mathbf{i}, \mathbf{j}) defining an orthonormal basis where \mathbf{i} is aligned with the
98 direction of the surface wind, and θ is the angle between the surface wind and surface currents.
99 Renault et al. (2017, their supplementary information) show that the angle between the surface

current and e cannot exceed 19.5° , such that $|\mathbf{u}_o|e \approx |e|\mathbf{u}_o$. It can further be assumed that—when considering mesoscale and submesoscale surface currents— θ has a uniform random distribution¹ such that the surface stress anomaly can be approximated as (Renault et al. 2017),

$$\tau' \approx -\frac{3}{2}\rho_a c_d |\mathbf{U}_a| \mathbf{u}_o. \quad (4)$$

In the following discussion $\bar{\tau}$ is referred to as the background wind stress, and τ' as the anomaly due to the CFB. Note however that while the approximate form of the stress, (4), is used in scaling arguments and for conceptual discussion, calculations involving the numerical model rely on the full surface stress (1), or stress anomaly (2), without approximation. Importantly, it can be clearly seen from (4) that the CFB-induced stress anomaly acts to oppose surface currents, such that it acts as a sink of kinetic energy through the surface wind work term—the ‘eddy-killing’ effect of the CFB. It is shown below that this alignment of the stress anomaly with the surface currents also has dynamical and energetic consequences for submesoscale flows through the Ekman transport of buoyancy.

b. Ekman buoyancy flux

At fronts, winds generate an advective flux of buoyancy, defined as (Thomas and Ferrari 2008),

$$\text{EBF} = \frac{\tau \times \hat{k}}{\rho_o f} \cdot \nabla_h b, \quad (5)$$

where ρ_o is the density of seawater, b is the buoyancy, and ∇_h is the horizontal gradient operator. This can also be directly related to the wind-driven component of the surface PV flux, which goes as $J_{WIND} \approx f\text{EBF}/h$ where h is the depth of the well-mixed portion of the surface boundary layer (Thomas and Ferrari 2008; Wenegrat et al. 2018). When the winds are oriented in the ‘upfront’ direction (opposing the surface thermal wind shear) the transport is towards the dense-side of the front, acting as a buoyancy and PV source to the mixed-layer. In contrast ‘downfront’ winds in the direction of the surface thermal wind shear transport dense-water over light, driving turbulent mixing and destroying PV.

¹This assumption is taken only for conceptual simplicity, and is not strictly necessary as $|\mathbf{e}| = 1/2\sqrt{1+3\cos(\theta)^2}$ such that it is always on the interval (0.5, 1) (Renault et al. 2017).

¹²² Expanding the definition of the EBF using the wind-stress given by (1) and (2) shows how the
¹²³ CFB can modify the surface EBF

$$\text{EBF} = \underbrace{\frac{\bar{\tau} \times \hat{k}}{\rho_o f} \cdot \nabla_h b}_{\text{EBF}_{\bar{\tau}}} + \underbrace{\frac{\tau' \times \hat{k}}{\rho_o f} \cdot \nabla_h b}_{\text{EBF}_{\tau'}}. \quad (6)$$

¹²⁴ The strength of the CFB effect on EBF can be estimated using (4),

$$\text{EBF}_{\tau'} \approx - \left(\frac{3}{2} \frac{\rho_a}{\rho_o} \frac{c_d}{|f|} \right) |U_a| |u_o| |\nabla_h b| \cos \phi, \quad (7)$$

¹²⁵ where ϕ is the angle between the surface currents and the surface thermal wind shear.

¹²⁶ Equation (7) indicates that the CFB may generate significant buoyancy—and PV—fluxes in the
¹²⁷ presence of strong surface currents aligned with sharp fronts. For illustration, posing this as an
¹²⁸ effective Ekman heat flux ($\text{EHF} = \rho_o c_w \alpha^{-1} g^{-1} \text{EBF}$, where c_w is the specific heat of seawater and
¹²⁹ α is the thermal expansion coefficient) shows that the CFB can generate equivalent advective heat
¹³⁰ fluxes of $O(1000 \text{ W m}^{-2})$ at strong submesoscale fronts (using values observed in the Kuroshio
¹³¹ by D’Asaro et al. 2011, where $|U_a| \sim 10 \text{ m s}^{-1}$, $|u_o| \sim 1 \text{ m s}^{-1}$, and $|\nabla_h b| \sim 10^{-5} \text{ s}^{-2}$). Below it
¹³² is argued that the frequent alignment of surface currents and surface thermal wind shear implies
¹³³ that the CFB will generally reduce the downfront component of the surface wind-stress, acting to
¹³⁴ generate an effective *source* of buoyancy—and PV—to the mixed-layer.

¹³⁵ Finally, to further contextualize the importance of the CFB on EBF it is useful to compare the
¹³⁶ anomaly term to the standard formulation, which considers only the earth-relative wind speed. The
¹³⁷ ratio of the two is given by,

$$\frac{\text{EBF}_{\tau'}}{\text{EBF}_{\bar{\tau}}} \sim - \frac{U_o}{U_a} \frac{\cos \phi}{\cos \psi}, \quad (8)$$

¹³⁸ where U_o and U_a respectively scale the magnitude of the surface current and winds, and ψ is
¹³⁹ the angle between the wind and the surface thermal wind shear. This ratio also scales the relative
¹⁴⁰ importance of the CFB to background wind-driven PV fluxes. Notably, (8) does not depend directly
¹⁴¹ on the strength of the buoyancy gradient, and instead depends only on the relative magnitudes of
¹⁴² the surface current and wind speed, and their alignment with the front. Generally the ratio of the
¹⁴³ velocity magnitudes will be small, although not always negligibly so in cases of weak or moderate

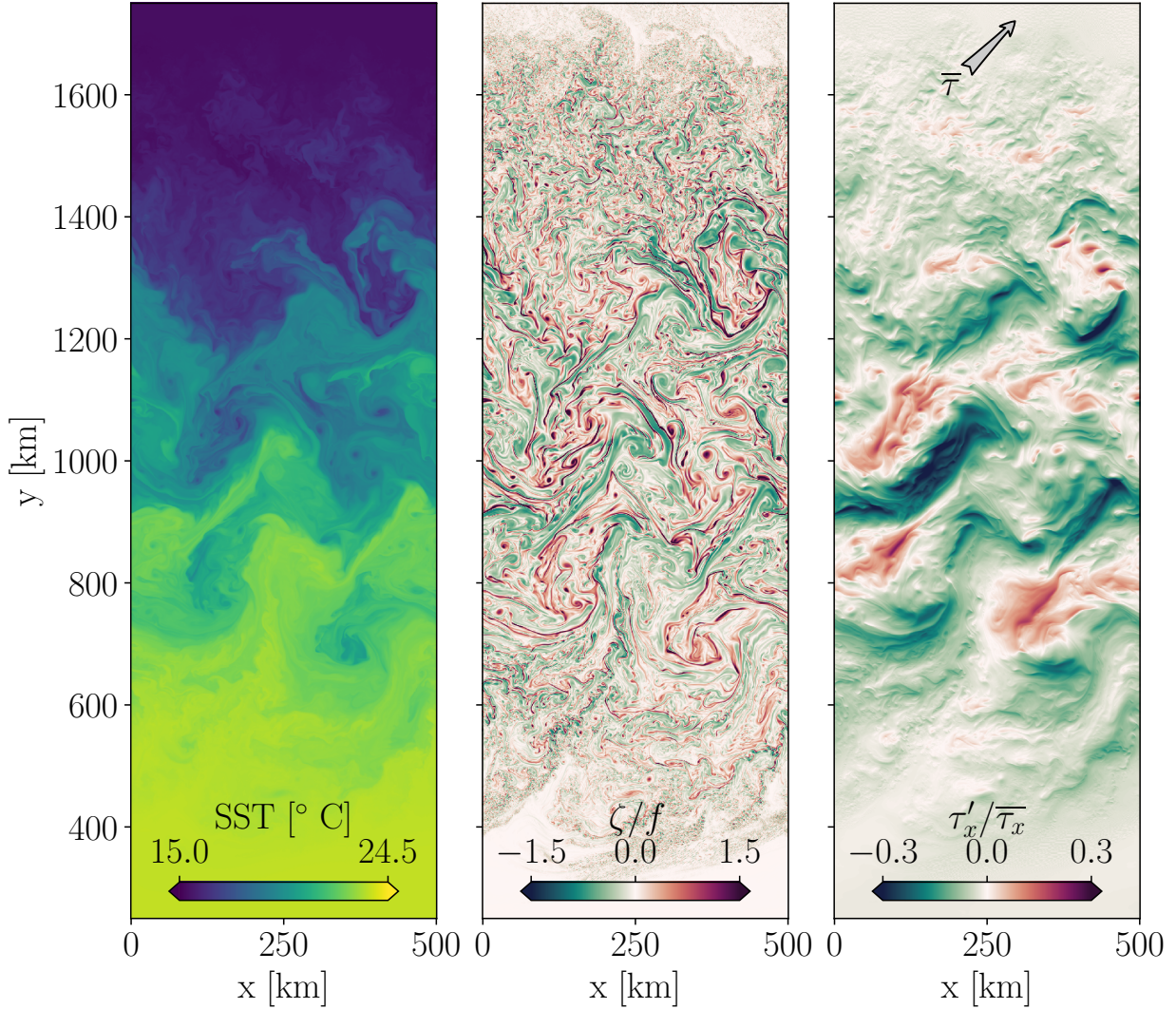
winds and strong surface flows. However despite this, the tendency of surface currents to align with fronts (ie. for ϕ to be small) allows the CFB contribution to play an important role in cases where winds and fronts are not aligned, or when integrating across many fronts where $EBF_{\bar{\tau}}$ is of alternating sign (such that $\int_A \cos \psi \, dA \approx 0$).

3. Results from numerical simulations

a. Description of simulations

Numerical simulations were performed using the Coastal and Regional Ocean COMmunity (CROCO) model (Auclair et al. 2022). The domain was configured as an idealized re-entrant channel, with 500 km length in the periodic x-direction, 2000 km in the y-direction (bounded by free-slip walls), and a uniform depth of 4000 m. The vertical direction was discretized with 100 stretched vertical levels, with near-surface resolution of $\Delta z = 3.6$ m, and the K-Profile Parameterization was used for the turbulence closure (KPP, Large et al. 1994). Existing turbulence closures are known to not accurately represent all pathways for the generation of turbulence at fronts (Bachman et al. 2017; Chor et al. 2022), however exploration of the sensitivity of results to choice of turbulence closures is beyond the scope of the present work.

The flow was initialized in geostrophic balance, with a baroclinically unstable horizontal buoyancy gradient (a detailed description of the initial frontal configuration can be found in Soufflet et al. 2016). An alternate configuration with an imposed initial mixed-layer was tested and found to not qualitatively alter the results. The simulation was first allowed to evolve with no surface forcing for 360 days at mesoscale resolving resolution ($\Delta x = \Delta y = 2$ km), during which time the temperature front was maintained by relaxation towards the initial condition. At the end of the 360 day spin-up period there is an active field of mesoscale eddies, and the eddy kinetic energy has reached a quasi-steady state. The simulation was then restarted at submesoscale permitting resolution ($\Delta x = \Delta y = 500$ m), without relaxation, allowing the rapid growth of submesoscale mixed-layer instabilities, characterized by $O(1)$ Rossby numbers (figure 1). It is computationally prohibitive to run a domain of this size at sufficient resolution to directly resolve symmetric instabilities (SI), hence some of the discussion around the potential impacts of the CFB on boundary layer energetics are posed as hypotheses in section 4.

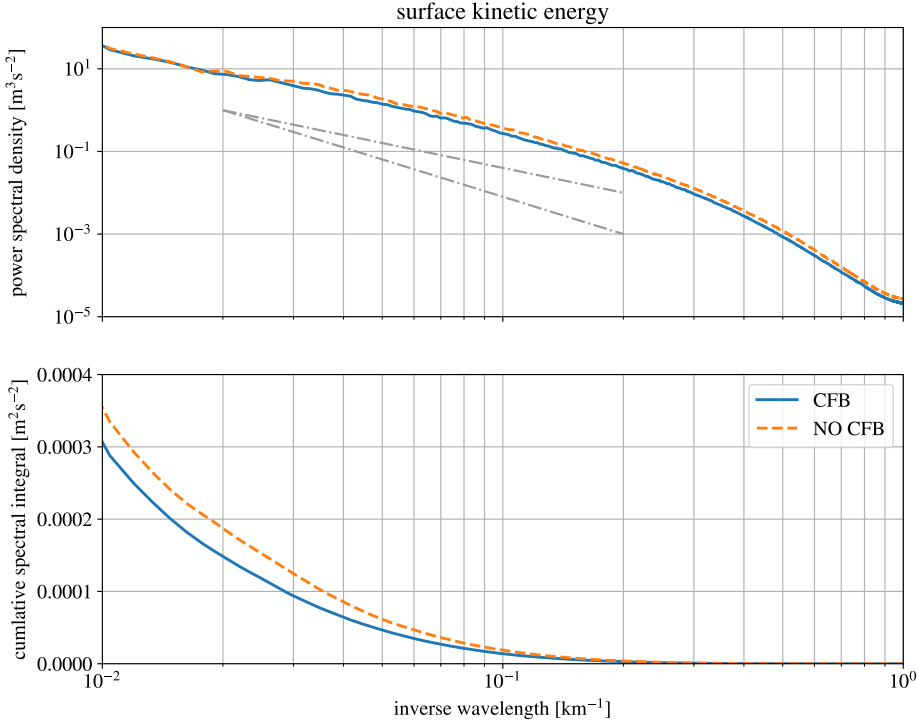


172 FIG. 1. Sea-surface temperature (left), surface relative vorticity normalized by the Coriolis frequency (center),
 173 and the zonal component of the wind-stress anomaly introduced by the current feedback normalized by the
 174 standard earth-relative formulation of the zonal wind-stress (right). The ocean surface velocity field imprints on
 175 the surface wind stress via the CFB mechanism, introducing correlations between surface currents, horizontal
 176 buoyancy gradients, and wind-stress. The background wind stress direction is indicated by the gray arrow. All
 177 fields are shown on day 385 (25 days after restart).

178 The high-resolution simulation was forced by a uniform surface heat loss of 25 W m^{-2} (unless
 179 otherwise noted) and a moderate surface wind of $|U_a| = 7 \text{ m s}^{-1}$ oriented towards the northeast
 180 direction. The surface stress was calculated using (1) with a constant drag coefficient of $c_d = 10^{-3}$.
 181 This simplified calculation of the surface stress isolates only the direct effect of the surface currents

on the wind-stress, and does not include other air-sea interaction mechanisms such as thermal feedbacks on the wind or drag coefficient, or the response of the winds to the CFB modifications in stress. This last mechanism in particular will tend to counter the CFB, as the reduction of surface stress due to the CFB can generate a partially compensating increase in surface winds (Renault et al. 2016b). This effect can be parameterized in uncoupled models by writing the relative wind vector as $\mathbf{U}_a - (1 - s_w)\mathbf{u}_o$ such that $s_w > 0$ accounts for the increase of the wind speed due to the CFB (Renault et al. 2016b). Noting that the perturbation stress is approximately linear in the surface current it follows that the magnitude of $\text{EBF}_{\tau'}$ would also be reduced by a factor of approximately $(1 - s_w)$ (as would other CFB effects such as the modification of the surface wind work). Estimates from a coupled global mesoscale resolving simulation suggest $s_w = 0 - 0.5$, with a global mean value of $s_w \approx 0.3$ (Renault et al. 2019b). However, it is not currently clear whether this value is representative of this effect at the submesoscale—where the small horizontal length scales limit the ability of the atmospheric boundary layer to respond locally (Wenegrat and Arthur 2018)—and so this effect is not directly estimated here. A high-resolution control simulation was also performed without the CFB (referred to as run ‘No-CFB’ throughout), such that the total wind-stress is given by $\bar{\tau}$ in equation (2).

Before discussing the EBF it is useful to first note several differences between the simulation with the CFB and the No-CFB control simulation without, although it is not implied these changes are solely attributable to changes in the EBF. Both simulations have kinetic energy spectral slope shallower than k^{-3} through the submesoscale (figure 2), consistent with realistic models and observations (Capet et al. 2008; Callies et al. 2015; Qiu et al. 2017; Soares et al. 2022). The amount of kinetic energy in the submesoscale is however reduced by approximately 15% in the CFB simulation. This tendency of the CFB to weaken the submesoscale is also reflected in the vorticity, divergence, and strain distributions (figure 3), which in each case show shifts towards zero in the distributions for the simulation run with the CFB. The surface vorticity in the CFB run shows considerably less negative values of vertical vorticity. Many of these features are also consistent with prior realistic simulations with the CFB, however an advantage of the idealized setup used here is that because both the CFB and No-CFB simulations are started from a common spin-up run—and only run for 30 days of simulation time—the mesoscale and larger flow remains relatively constant between the two runs with changes primarily in the emerging small-scales. This

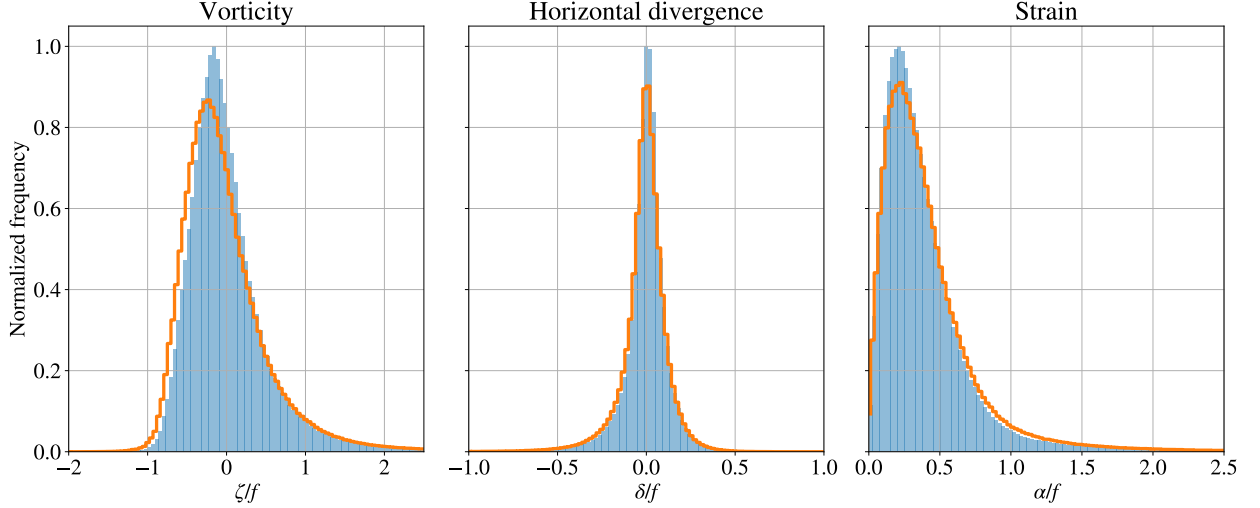


198 FIG. 2. Isotropic power spectral density of the surface kinetic energy averaged over days 380-390 (top panel),
199 comparing the run with the current feedback on stress (CFB) to the run without (No-CFB). Example k^{-2} and k^{-3}
200 spectral slopes are indicated by the dash-dot lines. The cumulative spectral integral (integrated from high to low
201 wavenumber) is shown in the bottom panel.

216 acts to isolate changes at the submesoscale, in contrast to longer integrations where changes to
217 the larger-scale circulation can generate indirect changes to the small-scale flow, in addition to the
218 direct effect of the CFB (Renault et al. 2018).

224 *b. Validation of approximate forms*

225 The numerical model is used to validate two of the approximations given in section 2, as shown
226 in figure 4. First is the approximate form of τ' , given in equation (4), which is compared to the
227 exact calculation formed by subtracting $\bar{\tau}$ from the full surface stress, eg. (2). Variance around
228 the 1-1 line is generally small, and reflects the joint contributions of the assumptions that terms
229 that are quadratic in the surface current are small, alignment of e and \mathbf{u}_o , and that the angle of
230 surface currents relative to the wind has a uniform random distribution. Equation (4) thus provides
231 a useful scaling of the strength of the CFB effect on the surface stress. The approximate form of the

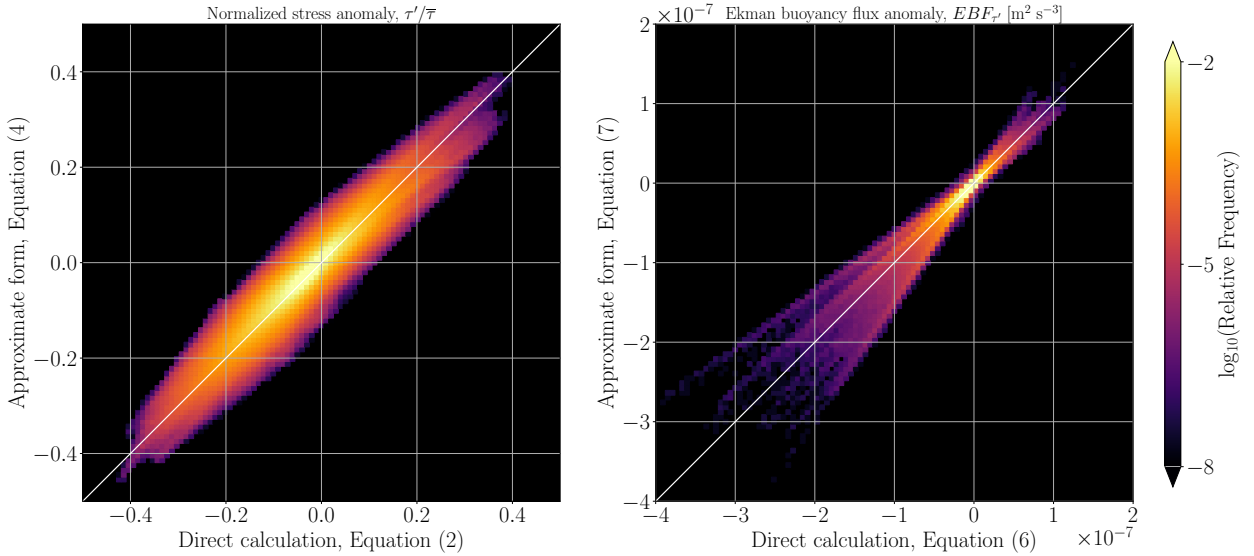


219 FIG. 3. Histograms of the surface vertical vorticity (left), surface horizontal divergence (center), and surface
 220 strain (right) comparing the simulation with the current feedback (CFB, blue) to the simulation run using only
 221 the earth-relative surface wind-stress (No-CFB, orange). In each plot the distributions are normalized by the
 222 peak value in the distribution of simulation CFB, the x-axis is normalized by the Coriolis frequency, and data
 223 covers the last 5 days of simulation time.

232 EBF $_{\tau'}$ given by (7) likewise is able to reasonably approximate the true values, a result that follows
 233 from it adding no additional assumptions beyond the approximate form of the stress. Errors in the
 234 approximate form increase at extreme values of EBF $_{\tau'}$, likely due to these values being controlled
 235 by just a few individual fronts such that the assumption used in deriving (4) of a uniform random
 236 distribution between surface currents and wind direction does not hold. The tendency of EBF $_{\tau'}$ to
 237 be negative (oriented downwards such that it is a source in the mixed-layer budget) is also evident,
 238 and is discussed further below.

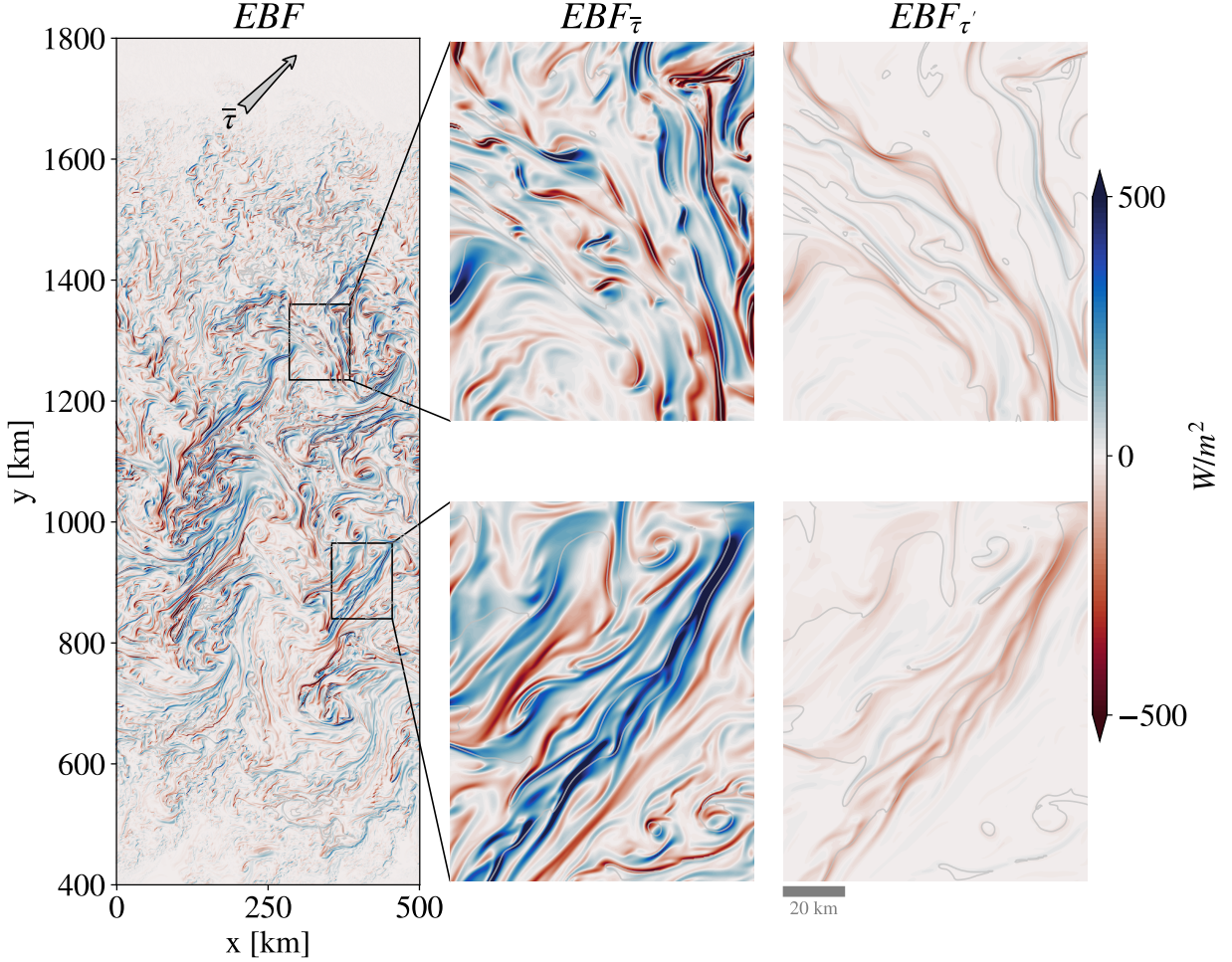
244 *c. Changes to the Ekman buoyancy flux*

245 A snapshot of the Ekman Buoyancy Flux is shown in figure 5, with units given as an equivalent
 246 heat flux for illustrative purposes. Values in this simulation reach extremes of $O(\pm 1000 \text{ W m}^{-2})$,
 247 again emphasizing how at fronts these terms can exceed typical air-sea buoyancy fluxes. The
 248 scaling for the CFB-induced EBF relative to the background EBF, (8), highlights two particular
 249 frontal configurations where EBF $_{\tau'}$ may be significant locally at fronts. The first is the case of
 250 winds and fronts that are not aligned, as highlighted in the top row of figure 5. Here the winds



239 Fig. 4. Comparison of numerical results with approximate forms from section 2. Left panel: CFB induced
 240 stress anomaly, normalized by the standard bulk stress calculated using earth-relative wind speeds. Both zonal
 241 and meridional components are included. Right panel: CFB induced Ekman buoyancy flux anomaly. In both
 242 panels the colorscale shows the relative frequency of occurrence over simulation days 365-390 (normalized such
 243 that the sum of all bins is one), and the 1-1 line is indicated in white.

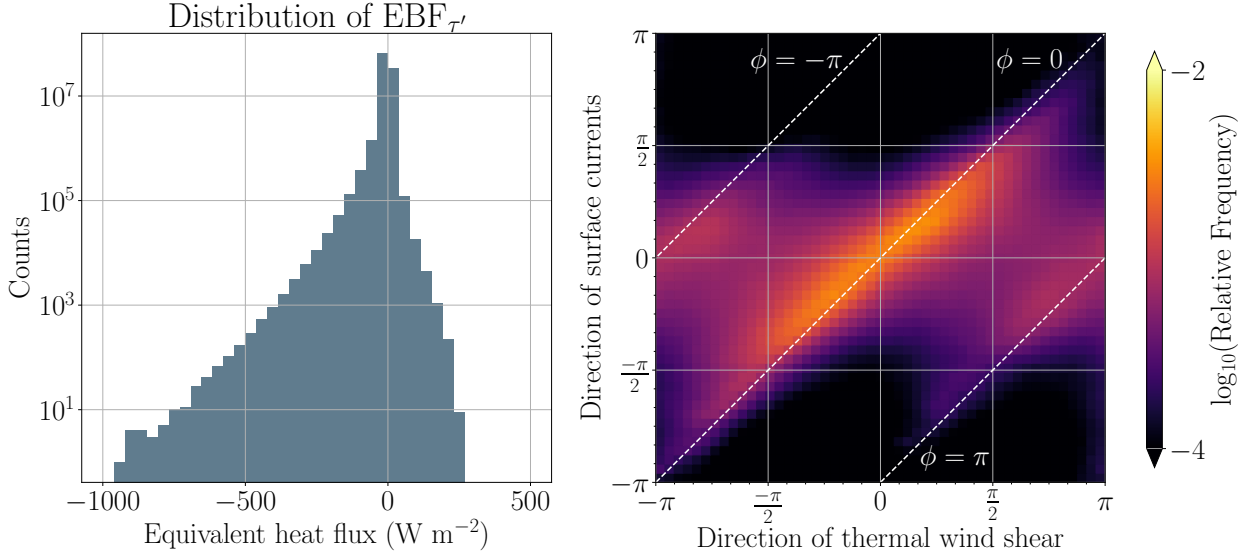
251 are blowing in a direction aligned with the surface buoyancy gradient (across-front winds), but the
 252 CFB effect contributes as much as 360 W m^{-2} of effective downward heat flux into the mixed-layer
 253 through the cross-frontal Ekman transport of buoyancy. This will act to restratify the front, and
 254 hence may suppress frontogenesis and the development of submesoscale instabilities through the
 255 associated surface PV injection. The other frontal configuration where scalings suggest significant
 256 contributions from $\text{EBF}_{\tau'}$ is the case of strong surface velocities, as shown in the bottom row of
 257 figure 5. Here the strong flow due to the large-scale meandering of the jet leads to large surface
 258 velocities ($\sim 1 \text{ m s}^{-1}$) that significantly reduce the stress. This acts as an effective *source* of
 259 downwards EBF to the mixed-layer, *reducing* the EBF due to downfront winds by approximately
 260 25% (an effective change in the equivalent Ekman heat flux of approximately 200 W/m^2). For this
 261 front the net EBF remains positive, representing a loss of buoyancy and PV at the surface, however
 262 as boundary layer properties such as the turbulent dissipation generated by symmetric instability
 263 are sensitive to the magnitude of this flux (Taylor and Ferrari 2010), the CFB contribution may



266 FIG. 5. The Ekman buoyancy flux from the numerical model (left panel) on day 385 (25 days after restart),
 267 along with two zoomed-in regions of the background $EBF_{\bar{\tau}}$ (center column) and the current feedback on stress
 268 induced anomaly $EBF_{\tau'}$ (right column). The colorscale is normalized to units of equivalent surface heat flux for
 269 illustrative purposes. Contours of surface temperature (thin gray lines), with 1°C intervals, are also shown to
 270 indicate frontal orientation (see also figure 1). The zoom regions are $100 \text{ km} \times 125 \text{ km}$ in the x and y directions,
 271 respectively, and a scale bar is shown.

264 be significant to the net rate of energy extracted from the geostrophic flow by downfront winds
 265 (section 4).

272 The distribution of all values of $EBF_{\tau'}$ is shown in figure 6. Values range from approximately
 273 -1000 W m^{-2} to 250 W m^{-2} , with a peak around 0 that reflects the spatial intermittency of fronts.
 274 The largest values are associated with those regions with both strong fronts and strong surface
 275 currents, where from (8) the stress anomaly term can contribute significantly to the total EBF (note



282 FIG. 6. Left: Distribution of the perturbation Ekman buoyancy flux, $EBF_{\tau'}$, with units given as an equivalent
 283 heat flux. Right: Joint distribution of the surface thermal wind shear direction (front direction) and the angle
 284 of the total surface currents. Angles are defined using the standard trigonometric convention. Cases of surface
 285 currents aligned with the surface thermal wind shear ($\phi = 0$), and opposing the surface thermal wind shear
 286 ($\phi = \pm\pi$), are indicated by the dashed white lines.

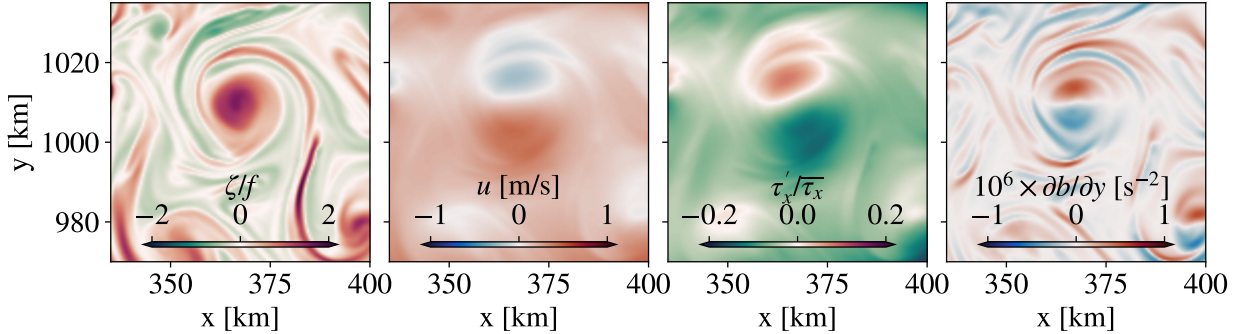
276 many regions where $|\tau'_x/\bar{\tau}_x| \gtrsim 0.3$ in figure 1). The distribution of $EBF_{\tau'}$ is negatively skewed (a
 277 pattern which is also evident in the predominantly negative values in the right columns of figures
 278 4 and 5). From (7) the sign of the perturbation EBF is set by the relative orientation of surface
 279 currents and fronts, with negative values resulting from surface currents that are in the direction
 280 of the thermal wind shear ($|\phi| < \pi/2$). The joint distribution of thermal wind shear and surface
 281 current directions is plotted in figure 6, indicating that they are largely parallel.

287 To what extent is this a general feature in the ocean? A heuristic argument can be made by
 288 noting that many ocean fronts result from frontogenesis by the surface strain field, leading to
 289 alignment of fronts and streamlines, and that these fronts in turn act to help set the direction
 290 of the surface flow through their thermal wind shear (Eliot and Wenegrat 2021). Indeed the
 291 general principle of the alignment of fronts and surface flows underpins some operational surface
 292 current retrieval algorithms (Isern-Fontanet et al. 2017). A more formal connection can be made
 293 via the relationship between the surface buoyancy and the geostrophic streamfunction in quasi-
 294 geostrophic dynamics, where in the specific case of surface quasi-geostrophic (SQG) flows the

surface buoyancy defines the streamfunction such that fronts and surface currents are identically aligned (Lapeyre 2017). Variants of the SQG model show skill at reproducing surface currents in models and observations (Klein et al. 2008; González-Haro and Isern-Fontanet 2014; González-Haro et al. 2020; Miracca-Lage et al. 2022), although observed kinetic energy spectra are generally inconsistent with SQG predictions (Callies and Ferrari 2013; Chereskin et al. 2019; Soares et al. 2022). In more dynamically complex settings, for instance layered quasi-geostrophic models that approximate the presence of a surface mixed layer, the total surface flow is a horizontal-scale dependent function of buoyancy anomalies at multiple levels (Callies et al. 2016).

This suggests an interpretation of $\text{EBF}_{\tau'}$ as primarily acting as a source term (in buoyancy and PV) to the mixed layer, and it is straightforward to further simplify both (7) and (8) using an assumption of $\phi = 0$. However, it can also be seen that there are some regions where the surface flow opposes the surface thermal wind shear ($\phi = \pm\pi$), flipping the sign of $\text{EBF}_{\tau'}$ (figures 5 and 6). These cases tend to occur in this simulation as a result of the strong eastward jet, which when superimposed on weaker baroclinic shear flows can cause the total surface velocity (jet plus eddy contributions) to oppose the thermal wind shear in some places. These instances are associated both with weaker fronts (where the thermal wind contribution to the flow is smaller), and with smaller velocities as the jet and thermal wind flows oppose each other in the total surface current. These factors both act to lower the magnitude of $\text{EBF}_{\tau'}$ (figure 6), limiting the impact of these events (compare for instance regions of positive vs negative $\text{EBF}_{\tau'}$ in figure 5), such that the occurrences of positive $\text{EBF}_{\tau'}$ contribute only about 20% to the total sum. As such, the remainder of this manuscript focuses largely on the case where $\phi \approx 0$ such that $\text{EBF}_{\tau'} < 0$.

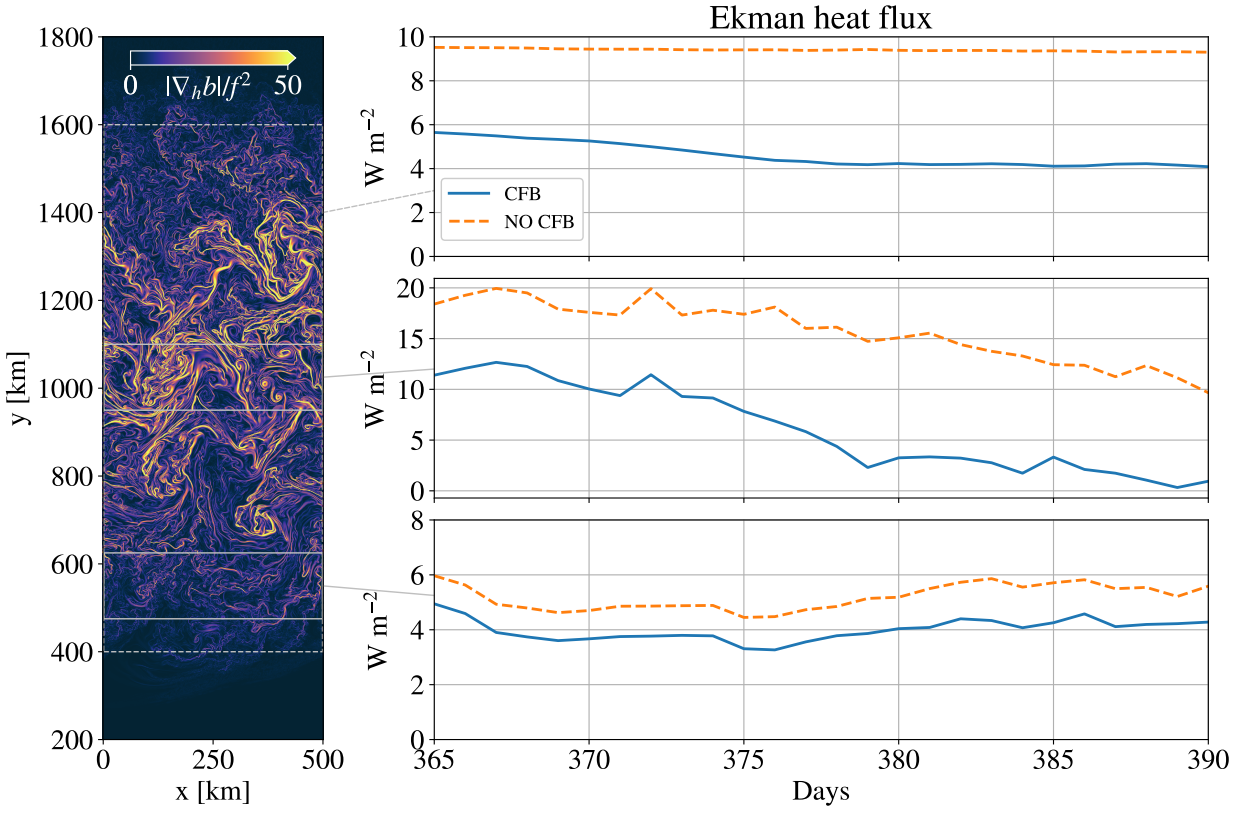
The covariability between surface currents and fronts (eg. figure 6) suggests that even weak surface currents may have area-integrated effects through the CFB. The best studied example of this is the so-called ‘eddy-killing’ effect, which can be seen in figure 7 which provides a zoomed in view of a single cyclonic eddy. The CFB induces stress anomalies that are anticorrelated with the surface currents, creating negative wind-work that drains eddy kinetic energy. However, it can also be seen that in this case the cold-core eddy is associated with a buoyancy gradient that is positively correlated with the stress anomaly (shown in figure 7 in terms of the meridional gradient relevant to the zonal stress anomaly, although both zonal and meridional components show a similar pattern). This pattern of covariability between τ' and $\nabla_h b$ indicates that $\text{EBF}_{\tau'} < 0$ when integrated across



327 FIG. 7. Zoomed in region highlighting a single submesoscale cyclonic eddy in terms of (from left to right)
 328 surface relative vorticity normalized by the Coriolis frequency, zonal surface current, zonal component of the
 329 stress anomaly, and the meridional buoyancy gradient. Anticorrelations between surface currents and wind-stress
 330 anomalies give rise to negative wind-work (eddy-killing effect), whereas correlations between stress anomalies
 331 and buoyancy gradients are associated with a negative Ekman buoyancy flux that acts as a source of buoyancy in
 332 the mixed-layer budget.

325 an eddy, in this case equivalent to an approximately -10 W m^{-2} surface heat flux. The mean $\text{EBF}_{\bar{T}}$
 326 over the eddy is about an order of magnitude smaller.

333 Integrating over larger areas likewise indicates a significant reduction of the total EBF by $\text{EBF}_{\tau'}$
 334 (figure 8). Over the whole frontal zone the total EBF is equivalent to an effective surface heat flux
 335 of $5-10 \text{ W m}^{-2}$, acting to cool the surface mixed layer, although these specific values are a function
 336 of the imposed mean wind and large-scale buoyancy gradient and hence cannot be generalized from
 337 these idealized simulations. More important is however the reduction of the area-integrated EBF
 338 by approximately 50% due to the CFB—a result that is predicted by (8) and the observed tendency
 339 for surface currents to be aligned with fronts. Similar results hold both within the center of the
 340 jet, where the flow is dominated by strong mesoscale features with large surface currents, and on
 341 the jet flanks where the fronts and flow are weaker and more isotropic (figure 8). In both cases
 342 the CFB reduces the area-integrated EBF, although this effect is less pronounced in the weaker-
 343 front region, consistent with the dependence of (8) on the strength of the surface currents. That
 344 these changes between the CFB and No-CFB runs in each case are due to $\text{EBF}_{\tau'}$ was confirmed
 345 by calculation of the integrated $\text{EBF}_{\bar{T}}$ from the CFB simulation, which also closely follows the
 346 No-CFB simulation (not shown), indicating there are not significant changes to the larger-scale
 347 mean horizontal buoyancy gradients between these runs.



348 FIG. 8. Magnitude of the surface horizontal buoyancy gradient (left panel) on day 385 (25 days after restart),
349 along with the spatial mean Ekman heat flux over the full frontal region (top, for $y=[400 \text{ km}, 1600 \text{ km}]$), a region
350 of strong fronts (middle, for $y=[950 \text{ km}, 1100 \text{ km}]$), and a region of weaker fronts (bottom, for $y=[475 \text{ km}, 625$
351 $\text{km}]$). The simulation run with the current feedback (CFB, solid blue line) can be compared to a simulation run
352 with the standard earth-relative formulation of the surface stress (NO-CFB, orange dashed line).

353 *d. Changes to the potential vorticity*

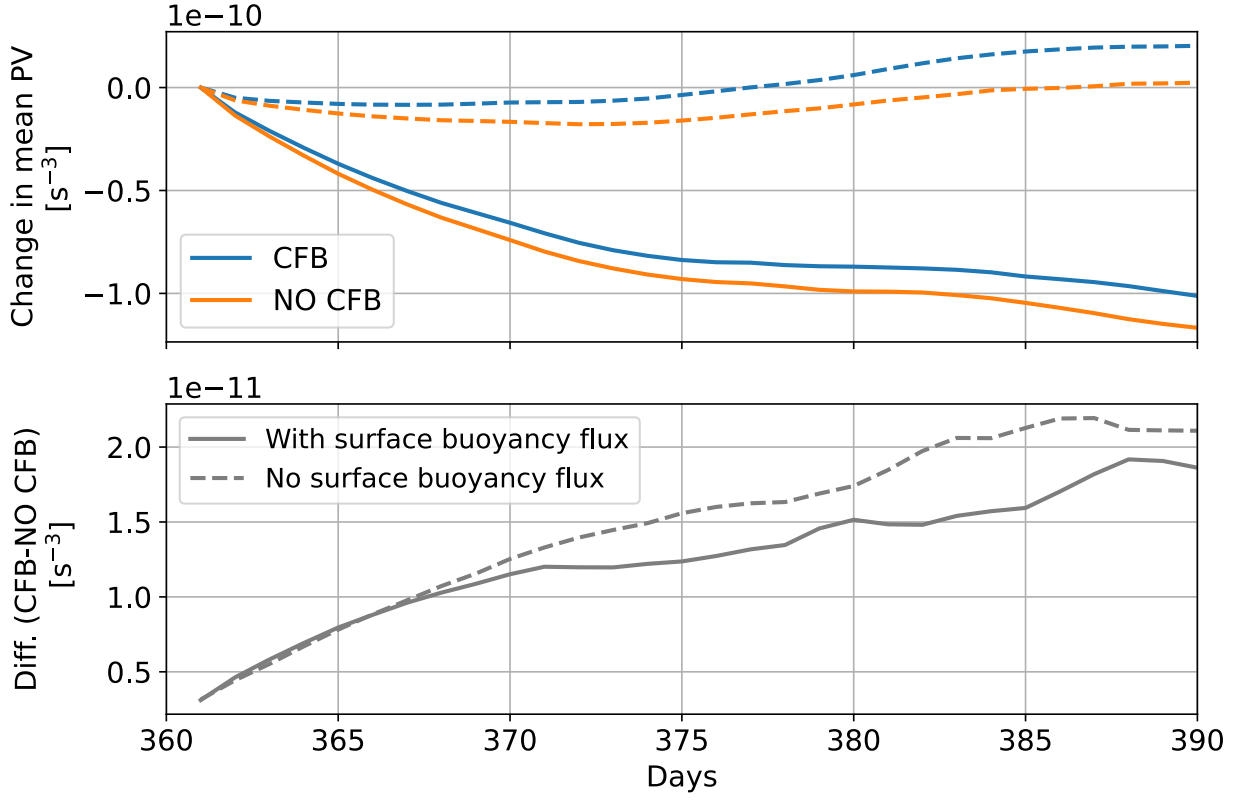
354 Finally, beyond the mixed-layer buoyancy budget, the EBF also affects the surface flux of Ertel
355 PV, which exerts strong dynamical controls on ocean circulation, both locally in the boundary layer
356 (Taylor and Ferrari 2010), and on the large-scale circulation as water masses are subducted into
357 the interior (Marshall et al. 2001; Wenegrat et al. 2018). The connection between the EBF and
358 surface PV flux at individual fronts is well established (Thomas and Ferrari 2008), and is thus not
359 reiterated here other than to note that the changes in EBF by $\text{EBF}_{\tau'}$ shown in figure 5 can also
360 be interpreted directly in terms of a reduction of PV destruction by the EBF (see also Chen et al.
361 2022, who found a reduction in PV destruction in a simulation of a single submesoscale eddy that

may be explained by the mechanism discussed here). Here it is noted that the cumulative effect of this reduction appears in the volume-integrated PV budget of these simulations (figure 9). In both the CFB and No-CFB cases PV is destroyed, largely due to the imposed surface heat loss which is approximately 5 times larger for this simulation configuration than the mean Ekman heat flux (figure 8). However the rate of PV destruction is reduced by approximately 15% when the CFB is included (this value includes the effect of the surface heat flux in the denominator). The CFB thus acts as an effective *source* of PV in these simulations (figure 9, bottom panel).

Simulations run with no surface buoyancy flux (CFB and No-CFB) are also shown for comparison (figure 9, dashed lines). The net evolution of the PV in this case is different, as expected without the strong (relative to the mean EBF) surface buoyancy loss acting to destroy PV. Notably without a surface buoyancy loss there is a net injection of PV in the case with the CFB, whereas the No-CFB case has a near-zero change over the simulation period. However, despite the differences in PV evolution, the change in the PV between CFB and No-CFB cases is very similar across the configurations with and without surface buoyancy fluxes (9, bottom panel). This effective PV injection by the CFB is consistent in sign and magnitude with the mean PV flux implied by $\text{EBF}_{\tau'}$ which can be very roughly estimated as $J_{\text{EBF}_{\tau'}} \sim f \text{EBF}_{\tau'} / h$ such that the change in volume-averaged PV over the 30 day simulation period goes as $\Delta q_{\text{EBF}} \sim -J_{\text{EBF}_{\tau'}} \Delta t / \Delta z \approx 2.7 \times 10^{-11} \text{ s}^{-3}$ (using $\text{EBF}_{\tau'}$ equivalent to a 5 W m^{-2} heat flux, an average mixed-layer depth of 45 m in the frontal zone, and a Δt of 30 days and Δz of 500 m for comparison with the cumulative change in figure 9, bottom panel). This estimate is similar to the actual volume-integrated PV change due to the CFB in both simulations, however a more complete attribution to $\text{EBF}_{\tau'}$ would require disentangling several mechanisms, and hence is beyond the scope of the present work (see discussion in section 4). Regardless, the changes in EBF and PV documented here suggest the CFB may be important in the PV budget both locally at fronts with strong surface currents or in cases of cross-frontal winds, and when considering the integrated contributions over many submesoscale fronts.

4. Discussion

The idealized simulations considered here are designed to provide a simple illustration of the direct effect of the CFB on the EBF. However, they are also associated with a number of limitations—specifically in resolution and realism—that do not allow quantification of a number of additional



387 FIG. 9. Comparison of the change in Ertel PV volume-averaged between the surface and 500 m depth and
 388 $y=500\text{--}1500 \text{ km}$ relative to day 361 ($V^{-1} \int_V q(t) - q(t_o) dV$). The top panel shows the change in mean PV relative
 389 to the PV on day 361 immediately following the simulation restart for the CFB run (solid blue) and the No-CFB
 390 run (solid orange). The bottom panel shows the difference in between the runs with and without the CFB. Results
 391 of a simulation run with no surface buoyancy flux are also shown (dashed lines in each subplot) for comparison.

396 aspects of how the CFB effect on EBF may be important for submesoscale dynamics and energetics.
 397 Several of these other mechanisms, and challenges for disentangling their effects, are discussed
 398 here.

399 Perhaps the most important limitation of the simulations considered in this manuscript is that they
 400 are not sufficiently high-resolution to permit symmetric instabilities, such that the direct energetic
 401 effects of $\text{EBF}_{\tau'}$ in the simulations cannot be usefully quantified. However, the reduction in surface
 402 EBF by the CFB is expected to affect symmetric modes in two ways. First, as shown above, the
 403 $\text{EBF}_{\tau'}$ acts primarily as a source term in the PV budget, which will tend to suppress the emergence
 404 of symmetric instabilities, potentially reducing the frequency of their occurrence. The net effect of
 405 this will vary depending on the forcing and how close to marginally stable to SI the fronts are, and

406 cannot be estimated a priori. Second, in the case of fronts where the net EBF remains positive (ie.
 407 wind-driven PV destruction), the CFB will modify the magnitude of the energy extracted from the
 408 balanced flow through the geostrophic shear production (GSP) which scales with the EBF (Taylor
 409 and Ferrari 2010; Thomas et al. 2013). This energy is ultimately cascaded forward to turbulence
 410 (Chor et al. 2022), and hence the CFB is expected to act to reduce the SI-enhancement of turbulent
 411 dissipation by an amount

$$\overline{\text{GSP}}' \approx \text{EBF}_{\tau'} \frac{h}{2} \approx -\frac{3}{4} \frac{\rho_a}{\rho_o} c_d |\mathbf{U}_a| |\mathbf{u}_o| |\Delta \mathbf{u}_g|, \quad (9)$$

412 where the overline indicates a vertical average over the mixed-layer of depth h , $|\Delta \mathbf{u}_g| = h |\nabla_h b| / f$
 413 is the magnitude of the change in geostrophic velocity over the mixed-layer and it is assumed $\phi = 0$.
 414 For the observations of symmetric instability along the Kuroshio discussed in section 2 (D’Asaro
 415 et al. 2011), the strong surface currents ($|\mathbf{u}_o| \approx 1.5$ m/s) and modest winds ($|\mathbf{U}_a| \approx 10$ m/s) imply
 416 that $\text{EBF}_{\tau'}$ could reduce the vertically-integrated turbulent dissipation rate by $O(10^{-5}$ W m kg $^{-1}$),
 417 about 15% of the total.

418 The CFB modification of the EBF may therefore act to reduce the rate of energy flux from
 419 the balanced flow to the submesoscale and dissipation, both through PV injection—which will
 420 reduce the frequency of symmetric instability—and through a direct modification of the growth
 421 rates via the change in EBF. This reduction of shear production and dissipation by SI can be
 422 compared to the loss of energy through the CFB wind-work anomaly, which goes as $\rho_o^{-1} \boldsymbol{\tau}' \cdot \mathbf{u}_o \approx$
 423 $-(3/2) \rho_o^{-1} \rho_a c_d |\mathbf{U}_a| |\mathbf{u}_o|^2$. It is therefore anticipated that even in SI unstable conditions, the CFB
 424 will slow the instability growth rate through both a reduction in the GSP and the generation of
 425 negative wind-work, with relative contributions dependent on the ratio of $|\Delta \mathbf{u}_g| / |\mathbf{u}_o|$.

426 Aside from the limitations of resolution, it is also worth highlighting the challenge—even in
 427 these relatively simple numerical experiments—of definitively partitioning the observed changes
 428 in the submesoscale (see for instance figures 2 and 3) across the various processes affected by the
 429 CFB. An illustrative example of this challenge comes from considering the change in PV between
 430 the CFB and No-CFB runs (figure 9), which will be affected both by the $\text{EBF}_{\tau'}$, and by changes to
 431 the strength of the Turbulent Thermal Wind (TTW) secondary circulations driven by the mixing
 432 of geostrophic momentum at fronts (Wenegrat and McPhaden 2016; McWilliams 2017). The PV
 433 fluxes associated with the TTW flow depends on $|\nabla_h b|^2$ (Wenegrat et al. 2018), and therefore may

434 be sensitive to changes in the strength of submesoscale fronts introduced by the CFB, including
435 changes forced directly by the $\text{EBF}_{\tau'}$ as well as those resulting from the reduction of mesoscale
436 and submesoscale eddy kinetic energy by the surface wind work. Direct diagnosis of the relative
437 contributions of changes in the EBF and TTW PV flux are confounded by both appearing in the
438 PV budget via the same frictional flux terms, such that disentangling the mechanisms may require
439 the design of more sophisticated numerical experiments than simple comparisons of runs with and
440 without the CFB.

441 Finally, despite this challenge it is however worth noting that the simulations used here show
442 a very slight *reduction* of the magnitude of the horizontal buoyancy gradients in the CFB run
443 (approximately 5%). This implies a reduction of TTW PV injection in the CFB case that is
444 inconsistent with the observed increase in PV of the simulations with the CFB relative to No-
445 CFB (figure 9), whereas the sign of the mean $\text{EBF}_{\tau'}$ is of the correct sense to inject PV. The
446 balance of these terms—particularly in realistic settings where models show that weakening of
447 the mesoscale circulation by the CFB can lead to significant increases in baroclinic conversion
448 of available potential energy by the submesoscale (Renault et al. 2018)—is not easily predicted.
449 Given the interdependence of various dynamical properties of the submesoscale (including eddy
450 buoyancy fluxes, TTW circulation, and the EBF) on common parameters such as the strength of
451 the horizontal buoyancy gradients, future work should consider both direct and indirect pathways
452 for air-sea interaction and coupling at the submesoscale.

453 5. Summary

454 In this manuscript a mechanism for the current feedback on the surface wind stress to affect
455 submesoscale ocean fronts is identified through the Ekman buoyancy flux. Scaling arguments
456 suggest that the CFB effect on the EBF can be significant in cases of strong surface currents,
457 or cross-frontal winds, with examples from a numerical simulation showing approximately 25%
458 changes in the local EBF due to the CFB. Importantly, this term acts primarily as a source of
459 buoyancy to the mixed-layer, or equivalently it acts to inject PV. This allows for even relatively
460 modest changes to the EBF at individual fronts to contribute a significant change to the area-
461 integral, reaching an approximately 50% reduction in the integrated EBF in the simulation shown
462 here. Considering the CFB modification of the EBF may therefore be important to understanding

463 the mixed-layer buoyancy budget at both individual fronts in some cases, and when considering
464 the integrated effects of the horizontal transport.

465 These changes can furthermore be directly related to changes in the frictional flux of PV, a key
466 determinant of submesoscale mixed-layer dynamics. The CFB is speculated to reduce both the
467 frequency of occurrence of submesoscale symmetric instabilities, and the rate at which they extract
468 and dissipate energy from the geostrophic flow field. Scaling arguments suggest that this mechanism
469 may have energetic effects that are similar in magnitude to the effects of the CFB on the surface
470 wind-work, and hence should be considered when looking at the energetic effects of the current
471 feedback at submesoscale fronts. These effects may be particularly important in considering PV
472 and buoyancy fluxes associated with submesoscale fronts embedded in more energetic mesoscale
473 features, where the surface currents can be large. Examples of this occur frequently in mesoscale
474 eddies, coastal fronts, and western boundary currents (Brannigan et al. 2017; D’Asaro et al. 2011;
475 Zhang and Qiu 2018; Wenegrat et al. 2020).

476 The transition from the ocean mesoscale to the submesoscale is not just a change in length-
477 scale, but rather represents a change in dynamical regimes (Taylor and Thompson 2023). This
478 indicates the possibility that other physical mechanisms of air-sea interaction may be active at
479 these scales, an example of which is the CFB modification of the EBF explored in this manuscript.
480 However, disentangling the direct effects of the change of EBF vs other mechanisms emerging from
481 the CFB on stress is challenging, even in the idealized numerical setup employed here. Further
482 challenging is the potential importance of indirect effects (for instance the effect of the CFB on the
483 TTW circulation and associated PV injection), which may have common parameter dependencies.
484 Progress on the understanding of submesoscale air-sea interaction will be aided by consideration
485 of the interplay of both direct and indirect effects of air-sea interaction processes, and how these
486 might change in the dynamical transition from mesoscale to submesoscale.

487 *Acknowledgments.* The author thanks Jim Carton, Leah Johnson, Dimitris Menemenlis, Leif
488 Thomas, and Ernesto Rodriguez for comments during preparation of this manuscript, and acknowl-
489 edges the University of Maryland supercomputing resources (<http://hpcc.umd.edu>) made available
490 for conducting the research reported in this paper. The input of two anonymous reviewers is also
491 gratefully acknowledged. This work is a contribution to the S-MODE project (Farrar et al. 2020), an
492 EVS-3 Investigation awarded under NASA Research Announcement NNH17ZDA001N-EVS3 and

493 NASA grant 80NSSC21K0554 awarded under NASA Research Announcement NNH20ZDA001N-
494 PO to the University of Maryland, College Park.

495 *Data availability statement.* No observational data was used in this work. The model output is
496 too large to be easily transferred, but can be made available on request. Model configuration and
497 analysis scripts will be made available through zenodo.org upon publication.

498 **References**

499 Auclair, F., and Coauthors, 2022: Coastal and Regional Ocean CCommunity model. Zenodo, URL
500 <https://zenodo.org/record/7415055>, <https://doi.org/10.5281/ZENODO.7415055>.

501 Bachman, S., B. Fox-Kemper, J. Taylor, and L. Thomas, 2017: Parameterization of Frontal
502 Symmetric Instabilities. I: Theory for Resolved Fronts. *Ocean Modelling*, **109**, 72–95,
503 <https://doi.org/10.1016/j.ocemod.2016.12.003>, URL <http://linkinghub.elsevier.com/retrieve/pii/S1463500316301482>.

505 Bishop, S. P., R. J. Small, and F. O. Bryan, 2020: The Global Sink of Available Potential
506 Energy by Mesoscale Air-Sea Interaction. *Journal of Advances in Modeling Earth Systems*,
507 **12** (10), <https://doi.org/10.1029/2020MS002118>, URL <https://onlinelibrary.wiley.com/doi/10.1029/2020MS002118>.

509 Brannigan, L., D. P. Marshall, A. C. Naveira Garabato, A. J. G. Nurser, and J. Kaiser, 2017: Sub-
510 mesoscale Instabilities in Mesoscale Eddies. *Journal of Physical Oceanography*, **47** (12), 3061–
511 3085, <https://doi.org/10.1175/JPO-D-16-0178.1>, URL <http://journals.ametsoc.org/doi/10.1175/JPO-D-16-0178.1>.

513 Bye, J. A., 1985: Large-Scale Momentum Exchange in the Coupled Atmosphere-Ocean. *Else-
514 vier Oceanography Series*, Vol. 40, Elsevier, 51–61, [https://doi.org/10.1016/S0422-9894\(08\)70702-5](https://doi.org/10.1016/S0422-9894(08)70702-5), URL <https://linkinghub.elsevier.com/retrieve/pii/S0422989408707025>.

516 Callies, J., and R. Ferrari, 2013: Interpreting Energy and Tracer Spectra of Upper-Ocean Turbulence
517 in the Submesoscale Range (1–200 km). *Journal of Physical Oceanography*, **43** (11), 2456–
518 2474, <https://doi.org/10.1175/JPO-D-13-063.1>, URL <http://journals.ametsoc.org/doi/10.1175/JPO-D-13-063.1>.

- 520 Callies, J., R. Ferrari, J. M. Klymak, and J. Gula, 2015: Seasonality in submesoscale tur-
521 bulence. *Nature Communications*, **6**, 6862, <https://doi.org/10.1038/ncomms7862>, URL <http://www.nature.com/doifinder/10.1038/ncomms7862>.
- 522
- 523 Callies, J., G. Flierl, R. Ferrari, and B. Fox-Kemper, 2016: The role of mixed-layer instabilities in
524 submesoscale turbulence. *Journal of Fluid Mechanics*, **788**, 5–41, <https://doi.org/10.1017/jfm.2015.700>, URL http://www.journals.cambridge.org/abstract_S0022112015007004.
- 525
- 526 Capet, X., J. C. McWilliams, M. J. Molemaker, and A. F. Shchepetkin, 2008: Mesoscale to
527 Submesoscale Transition in the California Current System. Part I: Flow Structure, Eddy Flux,
528 and Observational Tests. *Journal of Physical Oceanography*, **38** (1), 29–43, <https://doi.org/10.1175/2007JPO3671.1>, URL <http://journals.ametsoc.org/doi/abs/10.1175/2007JPO3671.1>.
- 529
- 530 Chen, X., W. Dewar, E. Chassignet, M. Bourassa, S. Morey, and G. Gopalakrishnan, 2022: On the
531 Feedback Between Air-Sea Turbulent Momentum Flux and Oceanic Submesoscale Processes.
532 *Journal of Geophysical Research: Oceans*, **127** (10), <https://doi.org/10.1029/2022JC018767>,
533 URL <https://onlinelibrary.wiley.com/doi/10.1029/2022JC018767>.
- 534
- 535 Chereskin, T. K., C. B. Rocha, S. T. Gille, D. Menemenlis, and M. Passaro, 2019: Characterizing the
536 Transition From Balanced to Unbalanced Motions in the Southern California Current. *Journal
of Geophysical Research: Oceans*, **124** (3), 2088–2109, <https://doi.org/10.1029/2018JC014583>,
537 URL <https://agupubs.onlinelibrary.wiley.com/doi/10.1029/2018JC014583>.
- 538
- 539 Chor, T., J. O. Wenegrat, and J. Taylor, 2022: Insights into the Mixing Efficiency of Sub-
540 mesoscale Centrifugal-Symmetric Instabilities. *Journal of Physical Oceanography*, **52** (10),
541 2273–2287, <https://doi.org/10.1175/JPO-D-21-0259.1>, URL <https://journals.ametsoc.org/view/journals/phoc/52/10/JPO-D-21-0259.1.xml>.
- 542
- 543 D'Asaro, E., C. Lee, L. Rainville, R. Harcourt, and L. Thomas, 2011: Enhanced Turbulence and
544 Energy Dissipation at Ocean Fronts. *Science*, **332** (6027), 318–322, <https://doi.org/10.1126/science.1201515>, URL <http://www.sciencemag.org/cgi/doi/10.1126/science.1201515>.
- 545
- 546 Dewar, W. K., and G. R. Flierl, 1987: Some Effects of the Wind on Rings. *Journal of Physical
Oceanography*, **17** (10), 1653–1667, [https://doi.org/10.1175/1520-0485\(1987\)017<1653](https://doi.org/10.1175/1520-0485(1987)017<1653):

- 547 SEOTWO>2.0.CO;2, URL [https://doi.org/10.1175/1520-0485\(1987\)017<1653:SEOTWO>2.0.CO;2](https://doi.org/10.1175/1520-0485(1987)017<1653:SEOTWO>2.0.CO;2).
- 548
- 549 Duhaut, T. H. A., and D. N. Straub, 2006: Wind Stress Dependence on Ocean Surface Velocity:
550 Implications for Mechanical Energy Input to Ocean Circulation. *Journal of Physical Oceanography*, **36** (2), 202–211, <https://doi.org/10.1175/JPO2842.1>, URL <http://journals.ametsoc.org/doi/10.1175/JPO2842.1>.
- 551
- 552
- 553 Elipot, S., and J. Wenegrat, 2021: Vertical structure of near-surface currents: Importance, state of
554 knowledge, and measurement challenges. *CLIVAR Variations*, **19**.
- 555
- 556 Farrar, J. T., and Coauthors, 2020: S-MODE: The Sub-Mesoscale Ocean Dynamics Experiment.
557 *IGARSS 2020 - 2020 IEEE International Geoscience and Remote Sensing Symposium*, IEEE,
558 Waikoloa, HI, USA, 3533–3536, <https://doi.org/10.1109/IGARSS39084.2020.9323112>, URL
<https://ieeexplore.ieee.org/document/9323112/>.
- 559
- 560 Ferrari, R., and C. Wunsch, 2009: Ocean Circulation Kinetic Energy: Reservoirs,
561 Sources, and Sinks. *Annual Review of Fluid Mechanics*, **41** (1), 253–282, <https://doi.org/10.1146/annurev.fluid.40.111406.102139>, URL <http://www.annualreviews.org/doi/10.1146/annurev.fluid.40.111406.102139>.
- 562
- 563 González-Haro, C., and J. Isern-Fontanet, 2014: Global ocean current reconstruction from
564 altimetric and microwave SST measurements. *Journal of Geophysical Research: Oceans*,
565 **119** (6), 3378–3391, <https://doi.org/10.1002/2013JC009728>, URL <http://doi.wiley.com/10.1002/2013JC009728>.
- 566
- 567 González-Haro, C., J. Isern-Fontanet, P. Tandeo, and R. Garello, 2020: Ocean Surface Currents
568 Reconstruction: Spectral Characterization of the Transfer Function Between SST and SSH.
569 *Journal of Geophysical Research: Oceans*, **125** (10), <https://doi.org/10.1029/2019JC015958>,
570 URL <https://onlinelibrary.wiley.com/doi/10.1029/2019JC015958>.
- 571
- 572 Isern-Fontanet, J., J. Ballabrera-Poy, A. Turiel, and E. García-Ladona, 2017: Remote sensing
573 of ocean surface currents: a review of what is being observed and what is being assimilated.
574 *Nonlinear Processes in Geophysics*, **24** (4), 613–643, <https://doi.org/10.5194/npg-24-613-2017>,
URL <https://npg.copernicus.org/articles/24/613/2017/>.

- 575 Johnson, L., C. M. Lee, E. A. D'Asaro, L. Thomas, and A. Shcherbina, 2020a: Restratification at
576 a California Current Upwelling Front. Part I: Observations. *Journal of Physical Oceanography*,
577 **50** (5), 1455–1472, <https://doi.org/10.1175/JPO-D-19-0203.1>, URL <https://journals.ametsoc.org/jpo/article/50/5/1455/345366/Restratification-at-a-California-Current-Upwelling>.
578
- 579 Johnson, L., C. M. Lee, E. A. D'Asaro, J. O. Wenegrat, and L. N. Thomas, 2020b: Restratification
580 at a California Current Upwelling Front. Part II: Dynamics. *Journal of Physical Oceanography*,
581 **50** (5), 1473–1487, <https://doi.org/10.1175/JPO-D-19-0204.1>, URL <http://journals.ametsoc.org/doi/10.1175/JPO-D-19-0204.1>.
582
- 583 Klein, P., B. L. Hua, G. Lapeyre, X. Capet, S. Le Gentil, and H. Sasaki, 2008: Upper Ocean
584 Turbulence from High-Resolution 3D Simulations. *Journal of Physical Oceanography*, **38** (8),
585 1748–1763, <https://doi.org/10.1175/2007JPO3773.1>, URL <http://journals.ametsoc.org/doi/10.1175/2007JPO3773.1>.
586
- 587 Lapeyre, G., 2017: Surface Quasi-Geostrophy. *Fluids*, **2** (1), 7, <https://doi.org/10.3390/fluids2010007>, URL <http://www.mdpi.com/2311-5521/2/1/7>.
588
- 589 Large, W. G., J. C. McWilliams, and S. C. Doney, 1994: Oceanic vertical mixing: A review and
590 a model with a nonlocal boundary layer parameterization. *Reviews of Geophysics*, **32** (4), 363,
591 <https://doi.org/10.1029/94RG01872>, URL <http://doi.wiley.com/10.1029/94RG01872>.
592
- 593 Luo, J.-J., S. Masson, E. Roeckner, G. Madec, and T. Yamagata, 2005: Reducing Climatology Bias
594 in an Ocean-Atmosphere CGCM with Improved Coupling Physics. *Journal of Climate*, **18** (13),
595 2344–2360, <https://doi.org/10.1175/JCLI3404.1>, URL <http://journals.ametsoc.org/doi/10.1175/JCLI3404.1>.
596
- 597 Marshall, J., D. Jamous, and J. Nilsson, 2001: Entry, Flux, and Exit of Potential Vorticity in
598 Ocean Circulation. *Journal of Physical Oceanography*, **31** (3), 777–789, [https://doi.org/10.1175/1520-0485\(2001\)031<0777:EFAEOP>2.0.CO;2](https://doi.org/10.1175/1520-0485(2001)031<0777:EFAEOP>2.0.CO;2), URL <http://journals.ametsoc.org/doi/abs/10.1175/1520-0485%282001%29031%3C0777%3AEFAEOP%3E2.0.CO%3B2>.
599
- 600 McWilliams, J. C., 2017: Submesoscale surface fronts and filaments: secondary circulation, buoy-
601 ancy flux, and frontogenesis. *Journal of Fluid Mechanics*, **823**, 391–432, <https://doi.org/10.1017/jfm.2017.480>.

- 602 jfm.2017.294, URL https://www.cambridge.org/core/product/identifier/S0022112017002944/type/journal_article.
- 603
- 604 Miracca-Lage, M., C. González-Haro, D. C. Napolitano, J. Isern-Fontanet, and P. S. Polito,
605 2022: Can the Surface Quasi-Geostrophic (SQG) Theory Explain Upper Ocean Dynamics
606 in the South Atlantic? *Journal of Geophysical Research: Oceans*, **127** (2), <https://doi.org/10.1029/2021JC018001>, URL <https://onlinelibrary.wiley.com/doi/10.1029/2021JC018001>.
- 607
- 608 Naveira Garabato, A. C., X. Yu, J. Callies, R. Barkan, K. L. Polzin, E. E. Frajka-Williams,
609 C. E. Buckingham, and S. M. Griffies, 2022: Kinetic Energy Transfers between Mesoscale
610 and Submesoscale Motions in the Open Ocean's Upper Layers. *Journal of Physical Oceanography*,
611 **52** (1), 75–97, <https://doi.org/10.1175/JPO-D-21-0099.1>, URL <https://journals.ametsoc.org/view/journals/phoc/52/1/JPO-D-21-0099.1.xml>.
- 612
- 613 Pacanowski, R. C., 1987: Effect of Equatorial Currents on Surface Stress. *Journal of Physical Oceanography*, **17** (6), 833–838, [https://doi.org/10.1175/1520-0485\(1987\)017<0833:EOECOS>2.0.CO;2](https://doi.org/10.1175/1520-0485(1987)017<0833:EOECOS>2.0.CO;2), URL [http://journals.ametsoc.org/doi/10.1175/1520-0485\(1987\)017<0833:EOECOS>2.0.CO;2](http://journals.ametsoc.org/doi/10.1175/1520-0485(1987)017<0833:EOECOS>2.0.CO;2).
- 614
- 615
- 616
- 617 Qiu, B., T. Nakano, S. Chen, and P. Klein, 2017: Submesoscale transition from geostrophic flows to
618 internal waves in the northwestern Pacific upper ocean. *Nature Communications*, **8** (1), 14 055,
619 <https://doi.org/10.1038/ncomms14055>, URL <https://www.nature.com/articles/ncomms14055>.
- 620
- 621 Rai, S., M. Hecht, M. Maltrud, and H. Aluie, 2021: Scale of oceanic eddy killing by wind from
622 global satellite observations. *Science Advances*, **7** (28), eabf4920, <https://doi.org/10.1126/sciadv.abf4920>, URL <https://www.science.org/doi/10.1126/sciadv.abf4920>.
- 623
- 624 Renault, L., P. Marchesiello, S. Masson, and J. C. McWilliams, 2019a: Remarkable Control
of Western Boundary Currents by Eddy Killing , a Mechanical Air-Sea Coupling Process.
625 *Geophysical Research Letters*, **46** (5), 2743–2751, <https://doi.org/10.1029/2018GL081211>, URL
626 <https://onlinelibrary.wiley.com/doi/abs/10.1029/2018GL081211>.
- 627
- 628 Renault, L., S. Masson, V. Oerder, S. Jullien, and F. Colas, 2019b: Disentangling the
Mesoscale Ocean-Atmosphere Interactions. *Journal of Geophysical Research: Oceans*, **124** (3),

- 629 2164–2178, <https://doi.org/10.1029/2018JC014628>, URL <https://onlinelibrary.wiley.com/doi/10.1029/2018JC014628>.
- 630
- 631 Renault, L., J. C. McWilliams, and J. Gula, 2018: Dampening of Submesoscale Currents by Air-Sea
632 Stress Coupling in the Californian Upwelling System. *Scientific Reports*, **8** (1), <https://doi.org/10.1038/s41598-018-31602-3>, URL <http://www.nature.com/articles/s41598-018-31602-3>.
- 633
- 634 Renault, L., J. C. McWilliams, and S. Masson, 2017: Satellite Observations of Imprint of Oceanic
635 Current on Wind Stress by Air-Sea Coupling. *Scientific Reports*, **7** (1), 17 747, <https://doi.org/10.1038/s41598-017-17939-1>, URL <http://www.nature.com/articles/s41598-017-17939-1>.
- 636
- 637 Renault, L., M. J. Molemaker, J. Gula, S. Masson, and J. C. McWilliams, 2016a: Control and
638 Stabilization of the Gulf Stream by Oceanic Current Interaction with the Atmosphere. *Journal of
639 Physical Oceanography*, **46** (11), 3439–3453, <https://doi.org/10.1175/JPO-D-16-0115.1>, URL
640 <http://journals.ametsoc.org/doi/10.1175/JPO-D-16-0115.1>.
- 641
- 642 Renault, L., M. J. Molemaker, J. C. McWilliams, A. F. Shchepetkin, F. Lemarié, D. Chelton,
643 S. Illig, and A. Hall, 2016b: Modulation of Wind Work by Oceanic Current Interaction with the
644 Atmosphere. *Journal of Physical Oceanography*, **46** (6), 1685–1704, <https://doi.org/10.1175/JPO-D-15-0232.1>, URL <https://journals.ametsoc.org/view/journals/phoc/46/6/jpo-d-15-0232.1.xml>.
- 645
- 646 Rooth, C., and L. Xie, 1992: Air-sea boundary layer dynamics in the presence of mesoscale surface
647 currents. *Journal of Geophysical Research*, **97** (C9), 14 431, <https://doi.org/10.1029/92JC01296>,
648 URL <http://doi.wiley.com/10.1029/92JC01296>.
- 649
- 650 Schubert, R., J. Gula, R. J. Greatbatch, B. Baschek, and A. Biastoch, 2020: The
651 Submesoscale Kinetic Energy Cascade: Mesoscale Absorption of Submesoscale Mixed
652 Layer Eddies and Frontal Downscale Fluxes. *Journal of Physical Oceanography*, **50** (9),
653 2573–2589, <https://doi.org/10.1175/JPO-D-19-0311.1>, URL <https://journals.ametsoc.org/view/journals/phoc/50/9/jpoD190311.xml>.
- 654
- 655 Seo, H., and Coauthors, 2023: Ocean Mesoscale and Frontal-Scale Ocean-Atmosphere Interac-
656 tions and Influence on Large-Scale Climate: A Review. *Journal of Climate*, **36** (7), 1981–2013,

- 656 https://doi.org/10.1175/JCLI-D-21-0982.1, URL <https://journals.ametsoc.org/view/journals/clim/36/7/JCLI-D-21-0982.1.xml>.
- 658 659 660 Shao, M., and Coauthors, 2019: The Variability of Winds and Fluxes Observed Near Submesoscale
Fronts. *Journal of Geophysical Research: Oceans*, 2019JC015236, <https://doi.org/10.1029/2019JC015236>, URL <https://onlinelibrary.wiley.com/doi/abs/10.1029/2019JC015236>.
- 661 662 663 664 Soares, S. M., S. T. Gille, T. K. Chereskin, E. Firing, J. Hummon, and C. B. Rocha, 2022:
Transition from Balanced to Unbalanced Motion in the Eastern Tropical Pacific. *Journal of Physical Oceanography*, **52** (8), 1775–1795, <https://doi.org/10.1175/JPO-D-21-0139.1>, URL <https://journals.ametsoc.org/view/journals/phoc/52/8/JPO-D-21-0139.1.xml>.
- 665 666 667 Soufflet, Y., P. Marchesiello, F. Lemarié, J. Jouanno, X. Capet, L. Debreu, and R. Benshila, 2016:
On effective resolution in ocean models. *Ocean Modelling*, **98**, 36–50, <https://doi.org/10.1016/j.ocemod.2015.12.004>, URL <http://linkinghub.elsevier.com/retrieve/pii/S1463500315002401>.
- 668 669 670 Su, Z., J. Wang, P. Klein, A. F. Thompson, and D. Menemenlis, 2018: Ocean submesoscales as a key component of the global heat budget. *Nature Communications*, **9** (1), <https://doi.org/10.1038/s41467-018-02983-w>, URL <http://www.nature.com/articles/s41467-018-02983-w>.
- 671 672 673 674 Sullivan, P. P., J. C. McWilliams, J. C. Weil, E. G. Patton, and H. J. S. Fernando, 2020: Marine Boundary Layers above Heterogeneous SST: Across-Front Winds. *Journal of the Atmospheric Sciences*, **77** (12), 4251–4275, <https://doi.org/10.1175/JAS-D-20-0062.1>, URL <https://journals.ametsoc.org/doi/10.1175/JAS-D-20-0062.1>.
- 675 676 677 Taylor, J. R., and R. Ferrari, 2010: Buoyancy and Wind-Driven Convection at Mixed Layer Density Fronts. *Journal of Physical Oceanography*, **40** (6), 1222–1242, <https://doi.org/10.1175/2010JPO4365.1>, URL <http://journals.ametsoc.org/doi/abs/10.1175/2010JPO4365.1>.
- 678 679 680 681 Taylor, J. R., and A. F. Thompson, 2023: Submesoscale Dynamics in the Upper Ocean. *Annual Review of Fluid Mechanics*, **55** (1), annurev-fluid-031422-095147, <https://doi.org/10.1146/annurev-fluid-031422-095147>, URL <https://www.annualreviews.org/doi/10.1146/annurev-fluid-031422-095147>.

- 682 Thomas, L., and R. Ferrari, 2008: Friction, Frontogenesis, and the Stratification of the Surface
683 Mixed Layer. *Journal of Physical Oceanography*, **38** (11), 2501–2518, <https://doi.org/10.1175/2008JPO3797.1>, URL <http://journals.ametsoc.org/doi/abs/10.1175/2008JPO3797.1>.
- 685 Thomas, L. N., and C. M. Lee, 2005: Intensification of Ocean Fronts by Down-Front Winds.
686 *Journal of Physical Oceanography*, **35** (6), 1086–1102, <https://doi.org/10.1175/JPO2737.1>,
687 URL <http://journals.ametsoc.org/doi/abs/10.1175/JPO2737.1>.
- 688 Thomas, L. N., J. R. Taylor, R. Ferrari, and T. M. Joyce, 2013: Symmetric instability in
689 the Gulf Stream. *Deep Sea Research Part II: Topical Studies in Oceanography*, **91**, 96–
690 110, <https://doi.org/10.1016/j.dsr2.2013.02.025>, URL <http://linkinghub.elsevier.com/retrieve/pii/S0967064513000829>.
- 692 Wenegrat, J. O., and R. S. Arthur, 2018: Response of the Atmospheric Boundary Layer to Subme-
693 soscale Sea Surface Temperature Fronts. *Geophysical Research Letters*, **45** (24), 13,505–13,512,
694 <https://doi.org/10.1029/2018GL081034>, URL <http://doi.wiley.com/10.1029/2018GL081034>.
- 695 Wenegrat, J. O., and M. J. McPhaden, 2016: Wind, Waves, and Fronts: Frictional Effects in a
696 Generalized Ekman Model. *Journal of Physical Oceanography*, **46** (2), 371–394, <https://doi.org/10.1175/JPO-D-15-0162.1>, URL <http://journals.ametsoc.org/doi/abs/10.1175/JPO-D-15-0162.1>.
- 697 Wenegrat, J. O., L. N. Thomas, J. Gula, and J. C. McWilliams, 2018: Effects of the Submesoscale
698 on the Potential Vorticity Budget of Ocean Mode Waters. *Journal of Physical Oceanography*,
700 **48** (9), 2141–2165, <https://doi.org/10.1175/JPO-D-17-0219.1>, URL <http://journals.ametsoc.org/doi/10.1175/JPO-D-17-0219.1>.
- 703 Wenegrat, J. O., L. N. Thomas, M. A. Sundermeyer, J. R. Taylor, E. A. D'Asaro, J. M.
704 Klymak, R. K. Shearman, and C. M. Lee, 2020: Enhanced mixing across the gyre boundary
705 at the Gulf Stream front. *Proceedings of the National Academy of Sciences*, **117** (30), 17 607–
706 17 614, <https://doi.org/10.1073/pnas.2005558117>, URL <https://pnas.org/doi/full/10.1073/pnas.2005558117>.

- 708 Xu, C., X. Zhai, and X.-D. Shang, 2016: Work done by atmospheric winds on mesoscale
709 ocean eddies. *Geophysical Research Letters*, **43** (23), 12,174–12,180, <https://doi.org/10.1002/2016GL071275>, URL <http://doi.wiley.com/10.1002/2016GL071275>.
- 710
- 711 Zhang, Z., and B. Qiu, 2018: Evolution of Submesoscale Ageostrophic Motions Through the Life
712 Cycle of Oceanic Mesoscale Eddies. *Geophysical Research Letters*, **45** (21), 11,847–11,855,
713 <https://doi.org/10.1029/2018GL080399>, URL <http://doi.wiley.com/10.1029/2018GL080399>.